

# Recent results of PADReS, the Photon Analysis Delivery and REDuction System, from the FERMI FEL commissioning and user operations

Marco Zangrando,<sup>a,b\*</sup> Daniele Cocco,<sup>c</sup> Claudio Fava,<sup>b</sup> Simone Gerusina,<sup>b</sup> Riccardo Gobessi,<sup>b</sup> Nicola Mahne,<sup>b</sup> Eric Mazzucco,<sup>b</sup> Lorenzo Raimondi,<sup>b</sup> Luca Rumiz<sup>b</sup> and Cristian Svetina<sup>b,d</sup>

Received 31 October 2014

Accepted 5 March 2015

Edited by I. Schlichting, Max Planck Institute for Medical Research, Germany

**Keywords:** photon transport; photon diagnostics; FEL.

<sup>a</sup>IOM-CNR, Laboratorio TASC, SS 14 km 163.5 in Area Science Park, 34149 Trieste, Italy, <sup>b</sup>Elettra – Sincrotrone Trieste SCpA, SS 14 km 163.5 in Area Science Park, 34149 Trieste, Italy, <sup>c</sup>SLAC National Accelerator Laboratory, 2575 Sand Hill Road, Menlo Park, CA 94025, USA, and <sup>d</sup>Graduate School of Nanotechnology, University of Trieste, Piazzale Europa 1, 34127 Trieste, Italy. \*Correspondence e-mail: marco.zangrando@elettra.eu

The Photon Analysis Delivery and REDuction System of FERMI (PADReS) has been routinely used during the machine commissioning and operations of FERMI since 2011. It has also served the needs of several user runs at the facility from late 2012. The system is endowed with online and shot-to-shot diagnostics giving information about intensity, spatial-angular distribution, spectral content, as well as other diagnostics to determine coherence, pulse length *etc.* Moreover, PADReS is capable of manipulating the beam in terms of intensity and optical parameters. Regarding the optics, besides a standard refocusing system based on an ellipsoidal mirror, the Kirkpatrick–Baez active optics systems are key elements and have been used intensively to meet users' requirements. A general description of the system is given, together with some selected results from the commissioning/operations/user beam time.

## 1. Introduction

The free-electron laser (FEL) FERMI started to deliver extreme ultraviolet/soft X-ray (EUV/SXR) photons in early 2011, becoming in late 2012 the first seeded FEL facility worldwide open to external users. It is endowed with two FELs covering the wavelength range from 100 to 4 nm in the fundamental harmonic and with full control of the polarization (Allaria *et al.*, 2014): 100–20 nm covered by FEL-1 and 20–4 nm by FEL-2. The machine operates at a repetition rate of 10 Hz, with the foreseen upgrade to 50 Hz that will take place in 2016. FEL-1 is fully operative and was used during the first three external users' runs (Allaria *et al.*, 2012). FEL-2, on the other hand, is ready to be opened to external users, having delivered during the commissioning a beam with the requested characteristics, especially in terms of energy per pulse, spectrum and general reliability (Allaria *et al.*, 2013a). In Table 1 the parameters for both FEL-1 and FEL-2 are reported. The machine scheme, the basic principles of the high-gain harmonic generation (HG), upon which the FEL emission is based, and the fresh bunch technique (used for FEL-2) are described elsewhere (Allaria *et al.*, 2010; Yu, 1991; Ben-Zvi *et al.*, 1992).

## 2. PADReS overview

PADReS consists of all the transport and diagnostics elements installed from ~30 m after the undulators to the experimental endstations (Zangrando *et al.*, 2009). The layout of the system

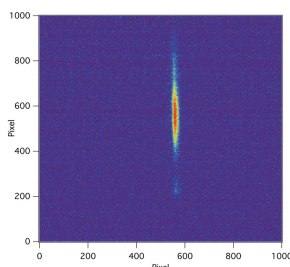


**Table 1**  
FEL-1 and FEL-2 parameters.

Parameter	Value		Units
	FEL-1	FEL-2	
Wavelength†	100–20	20–4	nm
Wavelength‡	100–17	20–4	nm
Pulse length (FWHM)§	30–100	<100	fs
Fractional bandwidth‡	$5 \times 10^{-4}$	$5 \times 10^{-4}$	
Polarization	Variable	Variable	
Repetition rate	10‡; 50†	10‡; 50†	Hz
Energy/pulse‡	>100	>30	μJ
Source size (FWHM)	290	140	μm
Divergence (r.m.s.)¶	1.25λ	1.5λ	μrad

† Design. ‡ Achieved. § Calculated. ¶ λ (nm).

is reported in Fig. 1. Each FEL presents a similar front-end section that includes a beam-defining aperture (BDA), two beam position monitors (BPMs), two intensity monitors (IOMs) and a gas absorber (GA). The latter, in particular, is

**Table 2**  
Parameters of the optics.

*d*, distance from the source (FEL-1/FEL-2); *w*, width; *l*, length; *θ*, grazing-incidence angle; Mat., coating material; Or., orientation (e.g. reflection plane); *R*, radius of curvature; RSE, residual tangential slope error r.m.s. All the optics are plane with the exception of the ellipsoidal mirror EM<sub>tmx</sub> on EIS-TIMEX. The KB mirrors on DiProI and LDM have a controllable optical shape going from plane to pseudo-elliptical. PM2a and SW<sub>ldm</sub> have two coatings, each covering half the width of the mirror, and their position can be adjusted laterally to select the coating.

Mirror	<i>d</i> (m)	<i>w</i> × <i>l</i> (mm)	<i>θ</i> (°)	Mat.	Or. (H or V)	<i>R</i> (km)	RSE (μrad)
PM1a	48.1/–	20 × 400	2.5	C	H	42.3	0.89
PM1b	54.3/–	20 × 250	5	C	H	10.6	0.56
PM2a	–/41.4	20 × 300	2.5	C/Au	H	28.1	0.95
ESP-LE	57.5/49.8	20 × 250†	2.5	C	H	29.7	0.44
ESP-HE	57.5/49.8	20 × 250†	2.5	Au	H	27.1	0.45
SW <sub>ldm</sub>	77.5/69.9	80 × 500	2	C/Ir	H	34	0.59
VD <sub>ldm</sub>	90.0/82.3	40 × 410	2	Au	V	154.6	0.32
KB-V <sub>ldm</sub>	95.6/87.9	40 × 400	2	Au	V	Variable	‡
KB-H <sub>ldm</sub>	96.1/88.5	40 × 400	2	Au	H	Variable	‡
VD <sub>dpi</sub>	94.5/86.8	40 × 410	2	Au	V	72	0.61
KB-V <sub>dpi</sub>	98.8/91.1	40 × 400	2	Au	V	Variable	‡
KB-H <sub>dpi</sub>	99.3/91.6	40 × 400	2	Au	H	Variable	‡
SW <sub>tmx</sub>	77.5/69.9	50 × 500	2	Au	H	300	0.35
EM <sub>tmx</sub>	92.5/84.8	20 × 390	2.5	Au	H	§	1.23

† Only the central 60 mm are ruled as grating. ‡ ≤0.5 μrad on any 70 mm-long portion of the surface. § (84840:1400) ellipsoidal shape.

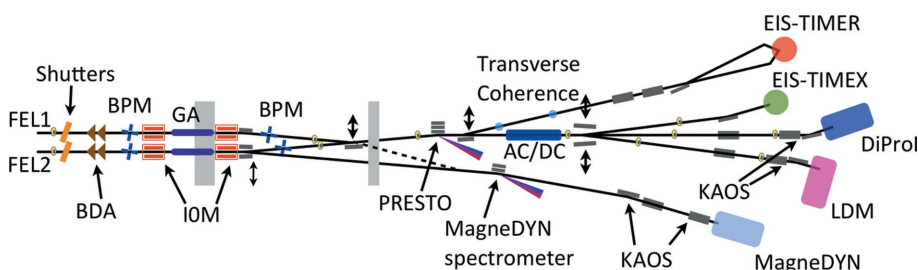


**Figure 1**  
The Photon Analysis Delivery and REduction System (PADReS) of FERMI. The first part, from the shutters to PRESTO, includes mostly diagnostic devices, together with plane mirrors. The central part includes the AC/DC and the transverse coherence setup, while in the last part of all the beamlines the refocusing systems are installed. For the acronyms used in the layout see the text.

capable of reducing the photon beam intensity in a controlled way by a factor of up to  $10^3$ – $10^4$ , and can be operated across the whole FERMI wavelength range using different gases such as N<sub>2</sub>, He, Ne, Xe or Kr (Rumiz *et al.*, 2011). A set of plane mirrors then follows (PM1a and PM1b for FEL-1, PM2a for FEL-2), and is used for both radiation safety issues and merging the optical paths of the two FELs. The energy spectrometer PRESTO (pulse-resolved energy spectrometer: transparent and online) is the first element in the experimental hall. It covers the wavelength ranges of both FELs with two diffraction gratings (ESP-LE and ESP-HE), sending the non-diffracted beam (0-order) to the beamlines, and using the diffracted part to determine the pulse spectral characteristics (Svetina *et al.*, 2011). All the mentioned diagnostics work on a shot-to-shot basis giving pulse-resolved information (tagged by the bunch number). A diagnostic devoted to transversal coherence measurements (not yet pulse-resolved) is installed along the EIS-TIMER branchline, while on the common path to the currently operative endstations (EIS-TIMEX, DiProI and LDM) an autocorrelator/delay creator (AC/DC) can provide information about pulse length. After AC/DC the photon beam finally travels through the refocusing mirror systems that are an ellipsoidal mirror for EIS-TIMEX (EM), and two Kirkpatrick–Baez (Kirkpatrick & Baez, 1948) active optics systems (KAOS) for both DiProI and LDM (Raimondi *et al.*, 2013; Capotondi *et al.*, 2013).

Aside from the currently operative endstations, two additional beamlines and their relative endstations will be installed in 2015–2016: EIS-TIMER and MagneDYN. They will not belong to the common path that already exists, as shown in Fig. 1. In particular, MagneDYN will be endowed with its own energy spectrometer and will reserve some space for a possible future installation of a dedicated split and delay line unit. EIS-TIMER will use several sets of toroidal refocusing mirrors to focus the photon beam into the endstation, while MagneDYN will employ a KAOS similar to those installed on LDM and DiProI.

Table 2 presents the general characteristics and the measured parameters of each optic in the transport system. In addition to the above-mentioned optics, other mirrors are described, such as: the switching mirrors deviating the beam to the branchlines (SW<sub>ldm</sub> and SW<sub>tmx</sub>), the vertical deflecting mirrors and the bendable mirrors of the KAOS-based branchlines (VD, KB-H and KB-V for

**Table 3**

Distances of PADReS elements from the sources (FEL-1/FEL-2).

The elements are duplicated for the two FEL lines until the YAG<sub>Safety-Hutch</sub>s. From that point the transport system is shared by the two sources. The AC/DC is composed of eight mirrors; thus only the central point distance is reported.

Element	$d_{\text{FEL-1}}/d_{\text{FEL-2}}$ (m)
YAG <sub>Undulator-Hall</sub>	32.5/24.8
Shutter	33/25.3
BDA	33.4/25.7
BPM-1	33.8/26.1
IOM-1	35/27.3
GA <sub>centre</sub>	41/33.3
IOM-2	46.6/38.9
BPM-2	50.6/43.5
YAG <sub>Safety-Hutch</sub>	53.6/45.6
AC/DC <sub>centre</sub>	71.2/63.6
YAG <sub>Experimental-Hall</sub>	72.8/65.2
Double slit <sub>Coherence</sub>	66.4/58.7
YAG <sub>Coherence</sub>	74.7/67

both LDM and DiProI branchlines), and the ellipsoidal re-focusing of EIS-TIMEX ( $EM_{\text{tmx}}$ ).

Finally, Table 3 presents the other elements composing PADReS, which are described in the following. For some of them a more detailed discussion is presented.

### 2.1. Beam-defining apertures

The BDAs are mechanically constituted by two excavated trunks of pyramid, each of them presenting a clear aperture of  $20 \times 20$  mm (Zangrando *et al.*, 2009). The pyramid geometry ensures that the FEL beam hits the copper walls of the BDA at a moderate incidence angle ( $7.6^\circ$ ), thus decreasing the fluence and avoiding damage. By moving the trunks transversally one with respect to the other it is possible to select the effective aperture defining the angular acceptance of the optical system, which then ranges from 0 to 0.6 mrad for FEL-1, and from 0 to 0.78 mrad for FEL-2.

### 2.2. Beam position monitors

Each BPM presents four metallic blades (made of copper) intercepting the tails of the transverse photon beam distribution and collecting a drain current proportional to the number of photons hitting them. When the photon beam distribution is stable (and Gaussian) it is possible to compute its centroid with a spatial resolution better than  $2 \mu\text{m}$  r.m.s. (Zangrando *et al.*, 2009). Having two BPMs, on each FEL, displaced by  $\sim 17$  m it is possible to determine the angular movement shot-by-shot with sub- $\mu\text{rad}$  precision.

### 2.3. Intensity monitors

The IOMs are installed, for each FEL, before and after the gas absorber, and are based on the photo-ionization of nitrogen at low particle density in the range  $10^{11} \text{ cm}^{-3}$  ( $p \sim 10^{-5}$  mbar): the gas becomes ionized by the incoming photon beam, and the generated ions are collected and counted (Zangrando *et al.*, 2009). The obtained signal, being proportional to the number of ionizing photons, is then used to derive the absolute number of photons per pulse. The IOMs, consequently, are almost completely transparent, do not suffer from

saturation effects and do not perturb the properties of the beam. Using cross-calibrated photodiodes, they were calibrated absolutely, and are routinely used to determine the intensity of the FEL beam with a few percent accuracy.

### 2.4. Transverse coherence

Along the branchline that finally brings the beam to the EIS-TIMER endstation, departing after the energy spectrometer, a simple Young's double-slit setup to determine the transverse coherence of the beam is installed. It consists of a set of vertical slits laser-cut into a copper foil (Double slit<sub>Coherence</sub>, placed at  $\sim 66.4$  m from FEL-1 and  $\sim 58.7$  m from FEL-2) mounted 8.3 m before a YAG screen collecting the interference patterns (YAG<sub>Coherence</sub>). Different slit separations are available from 0.8 up to 4 mm, and the slit width is  $40 \mu\text{m}$  for all of them, except for the 0.8 mm case where the width is  $20 \mu\text{m}$ . Preliminary results at 32.5 nm showed a good degree of transverse coherence, ranging from 90% at  $0.3\sigma$  (from the optical axis), to 50% at  $0.7\sigma$  (Zangrando *et al.*, 2012).

### 2.5. Autocorrelator/delay creator

On the common path before the three branchlines (LDM, DiProI and EIS-TIMEX) the AC/DC is installed. It is based on grazing-incidence Au-coated mirrors (four working at  $3^\circ$  for the 'pump', and four working at  $2^\circ$  for the 'probe' beams). The instrument can wavefront-split the incoming photon beam and then recombine it, after having introduced a controllable time delay between the two half-beams. In particular, by varying one of the two optical paths and keeping the other fixed, it is possible to obtain a delay ranging from  $-2$  to  $+30$  ps, with a minimum step size of the order of 10 fs. Preliminary tests were carried out successfully during the commissioning of AC/DC, but more dedicated experimental activity is foreseen for the near future.

### 2.6. Spatial and angular distribution monitors

Along PADReS several screens (Ce:YAG crystals, 25 mm diameter and 0.5 mm thickness, manufactured by Crytur) can be inserted to monitor the radiation in terms of spatio-angular distribution of the photon beam. Though invasive when used, they are mandatory during machine optimization as, in combination with the intensity monitors and the energy spectrometer, they provide information about the quality of the emission mode, the target being a  $TM_{00}$ -like mode. Figs. 2(a) to 2(d) report a typical evolution of the FEL emission optimization process where only when the emission is similar to that of (d) ( $TM_{00}$  mode-like) can the FEL emission process be considered optimized. Moreover, this optimization is also necessary to achieve the best focusing into the endstations. As evident from Fig. 2, when a non-ideal emission mode (Fig. 2e) is focused, the corresponding focus presents a shape (imaged by the indentation over a Si sample reported in Fig. 2f) that replicates the beam structures. In this particular case, the spurious structure on the side of the central Gaussian mode is visible both on the YAG screen and on the sample. On the other hand, when the emission mode is optimal the

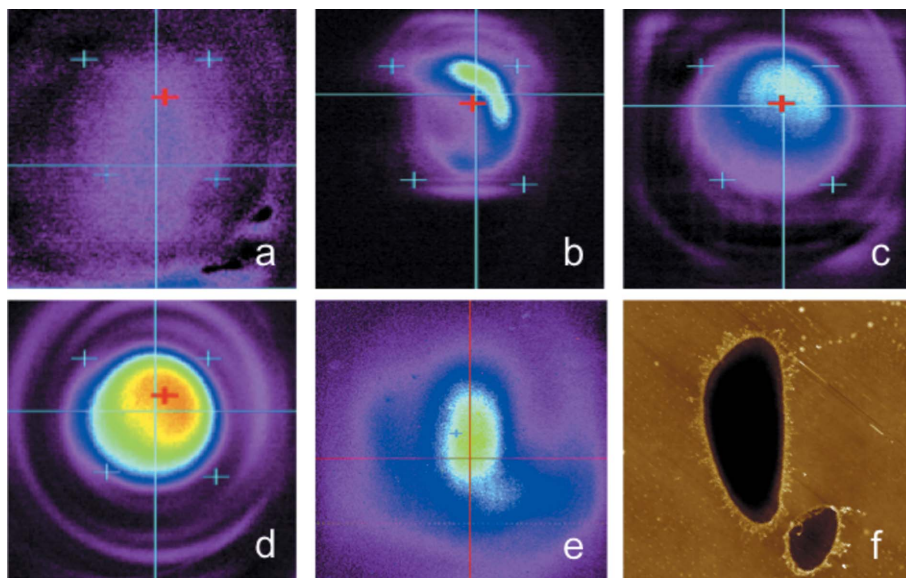


**Figure 2** (a)–(d) Evolution of the optimization of the FEL emission process, as monitored on a YAG screen placed along PADReS (YAG<sub>Safety-Hutch</sub>, ~54 m from the source). The mode quality is clearly increasing from left to right, following a proper tuning of the machine. (e) Non-optimal mode emission presenting a side structure that is recorded also in the focal spot, as shown in (f) where the indentation caused by the focus on a Si sample is reported.

focusing is also, and the generated focal spot is similar to that reported in the following (see §2.8).

### 2.7. Energy spectrometer PRESTO

**2.7.1. Spectral content and vertical distribution.** The energy spectrometer PRESTO covers the 100–3 nm range using two variable-line-spacing plane gratings whose parameters and optical characterization are reported elsewhere and not discussed here (Svetina *et al.*, 2011). Another variable-line-spacing grating will be implemented in 2015 to cover the low-wavelength part with better efficiency, giving the possibility to record the pulse spectrum with higher efficiency and in single-shot mode down to 3 nm. The instrument works online and shot-to-shot, delivers the specularly reflected radiation to the following beamlines, and horizontally focuses the diffracted part onto a YAG crystal (Ce:YAG crystals, 25 mm diameter and 0.5 mm thickness, manufactured by Crytur) imaged by a CCD camera (Hamamatsu C8800-01C high-resolution, 1000 × 1000, 12-bit). Using a standard high-resolution lens (Goyo Optical Inc.) the field of view of the CCD camera on the YAG is ~16 mm wide along the energy-dispersion direction (horizontal); at the same time, in the vertical direction the field of view is also ~16 mm. In the present configuration, limited by the 1000 8 μm pixels of the camera, the spectrum can be determined with a resolving power  $R$  above  $10^4$  on the whole range for both the gratings. Consequently, the FEL relative bandwidth (ranging from  $5 \times 10^{-4}$  to  $10^{-3}$ ) can be determined without any effect of the instrumental resolution of PRESTO. From the recorded image it is then possible to extract the spectral distribution of each pulse, online and non-invasively, simply by integrating verti-

cally the two-dimensional image (see Fig. 3). On the other hand, from the horizontal integration of the two-dimensional image recorded by the CCD camera it is also possible to obtain the vertical transverse spatial and angular distribution of the emitted radiation. In this way, at least for the vertical direction, it is possible to monitor the quality of the emission mode during the experiments, online and non-invasively (see Fig. 3).

**2.7.2. Two-pulse relative intensity monitor.** Besides the determination of the spectral content of the single FEL pulse, PRESTO has been used to characterize the emission of double FEL pulses during a two-colour experiment that will not be discussed here (Allaria *et al.*, 2013b). During that experiment, the FEL was seeded by two seed laser pulses at different wavelengths generating two FEL pulses at two different wavelengths with a temporal separation derived from the separation between

the seed laser pulses themselves: in that case it ranged in the interval 300–700 fs. Fig. 4(a) shows the typical acquisition obtained by PRESTO, always working online and on a shot-to-shot basis. From the image several details about the double-pulse generation could be inferred: first of all, the wavelength

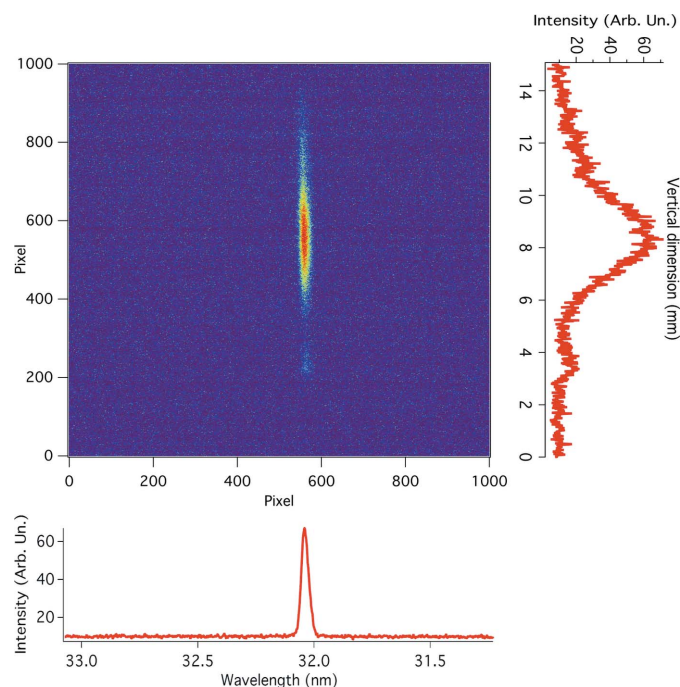


**Figure 3** Typical single-shot spectrum recorded by PRESTO. In this case the central emission energy of the FEL radiation was 32.05 nm. The histograms on the right and bottom report the spatial vertical distribution and the spectral distribution, respectively.

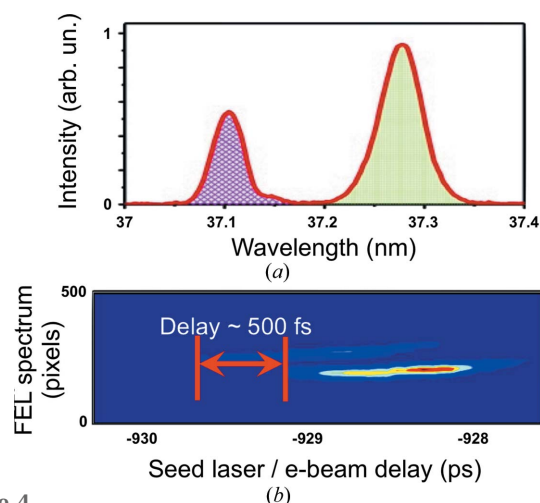


**Figure 4** (a) Spectral content and intensities of the two FEL pulses, characterized online by the energy spectrometer PRESTO in the two-colour double-pulse experiment. The purple and green areas were used to quantify the total intensity of each pulse impinging on the sample. (b) Onset of the pulse-splitting while scanning the relative time delay between the electron beam and the seed laser pulses along the modulator undulator (500 fs in this case).

separation of the two pulses ( $\sim 0.2$  nm, much greater than their bandwidths), as well as their spectral shape. Then, the relative and absolute (upon proper calibration) intensities of the two pulses were obtained, and this information was of utmost importance in the experiment, where a fluence-dependent pump–probe scheme was implemented, using one pulse as the pump and the other as the probe. In particular, given the possibility to selectively generate only one of the two FEL pulses by blocking one of the two seed laser pulses (used to start the HGHG FEL process), the intensity calibration was carried out using the intensity monitors along PADReS, and cross-checked with a calibrated bolometer installed on the DiProI endstation. This kind of information about the double pulse was even more valuable considering the fact that the temporal separation between the pulses was well below 1 ps, a timescale over which it is impossible to decouple the contribution of the two pulses using the FERMI gas-based I0 monitors, and generally very difficult using any other non-ultrafast diagnostic. Moreover, the use of PRESTO was fundamental in the monitoring of the onset of the double emission while seeding the electron bunch with the seed laser (double) pulse. In Fig. 4(b) a series of spectral distributions of the double (or single) pulse is reported along the vertical axis for a varying delay between the seed laser and the electron bunch (horizontal axis). This delay was controlled by a dedicated delay line in the seed laser transport system to the modulator undulator of FEL-1. As shown by the red bars, the onsets of the two single pulses were temporally displaced by 500 fs, and only the region where both pulses were present was used during the experiment.

## 2.8. Active refocusing system KAOS

The other crucial system along PADReS, besides PRESTO, is the refocusing section. In particular, two of the three

currently operative beamlines (DiProI and LDM), together with the upcoming MagneDYN beamline, need a dedicated optical system to focus the radiation meeting the following requests: (i) total decoupling between the horizontal and vertical focusing, (ii) perfect matching to the different source positions of FEL-1 and FEL-2 (longitudinally displaced  $\sim 7$  m, one with respect to the other), (iii) highest possible optical quality of the mirror surfaces in order to perturb the wavefront as little as possible, (iv) horizontal beam entering the endstations. The adopted solution at FERMI is to use a Kirkpatrick–Baez active optics system (KAOS) where two thin plane mirrors (thickness 10 mm) are bent by mechanical pushers to reach the desired curvature. This system is preceded by a vertical deflecting plane mirror ( $VD_{\text{ldm}}$  and  $VD_{\text{dpi}}$  for LDM and DiProI branchlines, respectively) so as to have a final photon beam direction parallel to the ground.

The focusing capabilities of KAOS have been tested during the commissioning phase and the user-dedicated runs from 2012 onwards, putting a strong effort in reaching the optical and mechanical limits of the system (Raimondi *et al.*, 2013). A representative result is reported in Fig. 5, where different approaches to the determination of the spot size are shown for a photon beam wavelength of 43 nm. In Fig. 5(a) the reconstruction from wavefront sensor (WFS) data is reported. The WFS (made by Imagine Optic) was placed behind the endstation, at about 1.2 m after the focal position, and the focus shape and distance from the instrument were derived. In particular, the obtained spot size was  $\sim 8 \mu\text{m} \times 9.5 \mu\text{m}$  FWHM, in fair agreement with the simulation performed using the *WISE* code (Raimondi *et al.*, 2013; Raimondi & Spiga, 2011, 2015). The code takes into account the diffraction limit, the physical optics and the measured mirror profiles, giving a spot size of  $\sim 5 \mu\text{m} \times 6 \mu\text{m}$  (Fig. 5b). These were confirmed by the post-mortem analysis of PMMA (polymethyl methacrylate) samples indented by the same radiation for which an estimation of  $\sim 10 \mu\text{m} \times 10 \mu\text{m}$  spot size was found (Figs. 5c, 5d).

Another important application of KAOS during the user activity at FERMI is the possibility, because it is optically active, to modify the focusing properties of the system. In particular, besides the capability of moderately changing the focal shape and size inside the FERMI endstations, it is possible to install additional experimental chambers on the back of the endstation in use, with respect to the FERMI photon beam arriving from the source: the residential endstation, thus, becomes a passing-through-only vacuum chamber. Quantitatively, the focal point can be moved by some metres downstream with respect to the nominal position inside the FERMI endstations, letting users perform the experiments within their chambers with a well focused beam. The best obtainable focus then depends on the fact that the demagnification factor changes as the focal arm of KAOS is increased, and  $\sim 20$ – $30 \mu\text{m}$  spot sizes can be obtained. The experience gathered so far has shown that focal spots created outside the FERMI endstations present transverse photon distribution patterns without noticeable inhomogeneities: full two-dimensional Gaussian distributions can be obtained upon

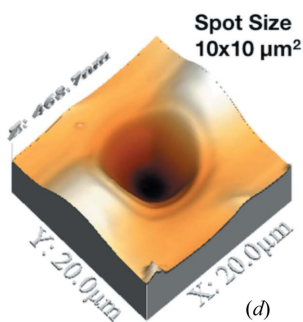
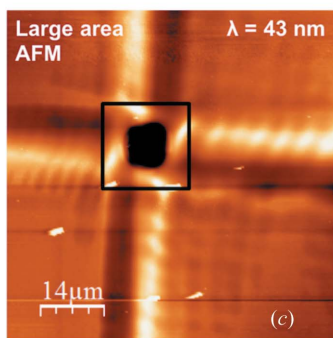
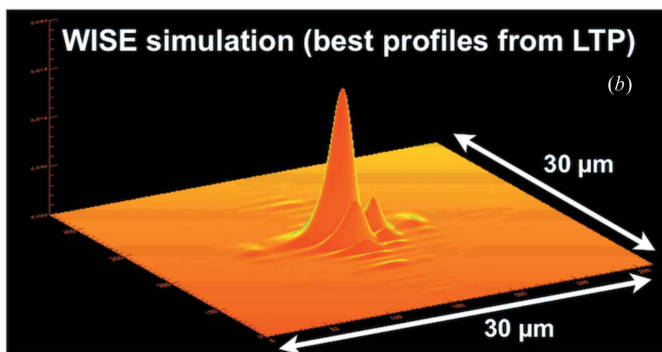
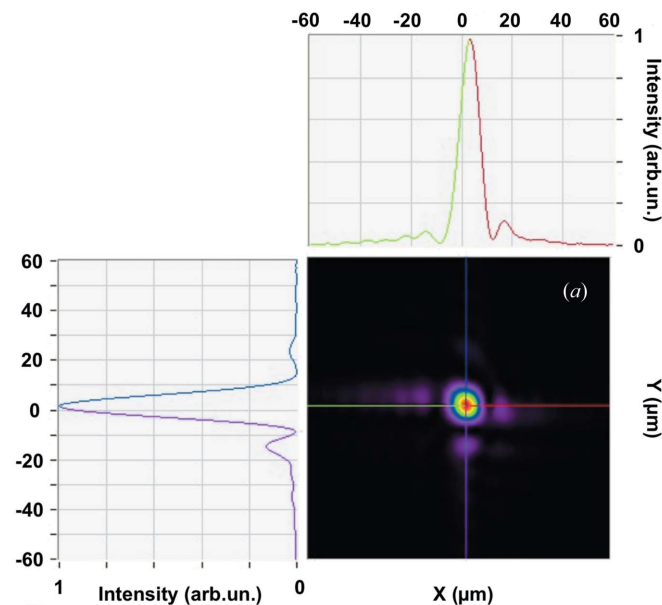


**Figure 5**  
KAOS spot-size determination by means of different techniques. (a) Reconstructed spot from wavefront sensor data. (b) Simulation with the WISE code of the focal spot, using the actual optical profiles of the two refocusing mirrors, as measured with a long trace profiler. (c) PMMA indentation post-mortem analysis of a focal spot created by KAOS. (d) Close-up of the image in (c).

proper WFS-based optimization. Finally, the KAOS mirrors can also be almost flattened in order to create a collimated photon beam whose dimensions depend on the wavelength in use and sit in the  $\sim 2\text{--}15$  mm range.

### 3. Conclusions

PADReS, the FERMI photon analysis, delivery and reduction system, is fully operative and has supported the activities of both the machine commissioning and the experimental users programs. As it determines and monitors several properties of the FEL photon beam, it represents an invaluable and unique resource to optimize the FEL emission and to characterize shot-to-shot the radiation used during the experiments carried out in the endstations. Besides more standard diagnostics like the intensity, position and transverse distribution monitors, some selected results from the energy spectrometer and the active optics refocusing systems have been presented and discussed.

### Acknowledgements

The authors would like to acknowledge the continuous and essential help of all the people involved in the FERMI@ Elettra project, and in particular the machine physics, the laser and the experimental endstations groups.

### References

Allaria, E. *et al.* (2012). *Nat. Photon.* **6**, 699–704.  
 Allaria, E. *et al.* (2013b). *Nat. Commun.* **4**, 2476.  
 Allaria, E. *et al.* (2013a). *Nat. Photon.* **7**, 913–918.  
 Allaria, E. *et al.* (2014). *Phys. Rev. X*, **4**, 041040.  
 Allaria, E., Callegari, C., Cocco, D., Fawley, W. M., Kiskinova, M., Masciovecchio, C. & Parmigiani, F. (2010). *New J. Phys.* **12**, 075002.  
 Ben-Zvi, I., Yang, K. M. & Yu, L. Y. (1992). *Nucl. Instrum. Methods Phys. Res. A*, **318**, 726–729.  
 Capotondi, F. *et al.* (2013). *Rev. Sci. Instrum.* **84**, 051301.  
 Kirkpatrick, P. & Baez, A. V. (1948). *J. Opt. Soc. Am.* **38**, 766–773.  
 Raimondi, L. & Spiga, D. (2011). *Proc. SPIE*, **8147**, 81470Z.  
 Raimondi, L. & Spiga, D. (2015). *Astron. Astrophys.* **573**, A22.  
 Raimondi, L. *et al.* (2013). *Nucl. Instrum. Methods Phys. Res. A*, **710**, 131–138.  
 Rumiz, L., *et al.* (2011). *Proceedings of the 2nd International Particle Accelerator Conference*, pp. 1530–1532.  
 Svetina, C., *et al.* (2011). *Proc. SPIE*, **8139**, 81390J.  
 Yu, L. Y. (1991). *Phys. Rev. A*, **44**, 5178–5193.  
 Zangrando, M., Abrami, A., Bacescu, D., Cudin, I., Fava, C., Frassetto, F., Galimberti, A., Godnig, R., Giuressi, D., Poletto, L., Rumiz, L., Sergio, R., Svetina, C. & Cocco, D. (2009). *Rev. Sci. Instrum.* **80**, 113110.  
 Zangrando, M., Abrami, A., Cocco, D., Fava, C., Gerusina, S., Gobessi, R., Mahne, N., Mazzucco, E., Raimondi, L., Rumiz, L., Svetina, C. & Parmigiani, F. (2012). *Proc. SPIE*, **8504**, 850404.